Input parameter ranking for neural networks in a space weather regression problem

Stefan Lotz[1,2][0000−0002−1037−348X], Jacques Beukes[2,3][0000−0002−6302−382X], and Marelie Davel[2,3][0000−0003−3103−5858]

[1] South African National Space Agency (SANSA), Space Science directorate, Hermanus, slotz@sansa.org.za
[2] Multilingual Speech Technologies, North-West University, South Africa
[3] Centre for Artificial Intelligence Research (CAIR), South Africa.
marelie.davel@nwu.ac.za, jpbeukes27@gmail.com

Abstract. Geomagnetic storms are multi-day events characterised by significant perturbations to the magnetic field of the Earth, driven by solar activity. Numerous efforts have been undertaken to utilise in-situ measurements of the solar wind plasma to predict perturbations to the geomagnetic field measured on the ground. Typically, solar wind measurements are used as input parameters to a regression problem tasked with predicting a perturbation index such as the 1-minute cadence symmetric-H (Sym-H) index. We re-visit this problem, with two important twists: (i) An adapted feedforward neural network topology is designed to enable the pairwise analysis of input parameter weights. This enables the ranking of input parameters in terms of importance to output accuracy, without the need to train numerous models. (ii) Geomagnetic storm phase information is incorporated as model inputs and shown to increase performance. This is motivated by the fact that different physical phenomena are at play during different phases of a geomagnetic storm.

Keywords: Space weather · Input parameter selection · Neural network

1 Introduction

Violent eruptions of electromagnetic energy (solar flares) and charged plasma (coronal mass ejections or CMEs) on the solar surface are propagated through interplanetary space and can impact the Earth's geomagnetic field. These perturbations can result in the disruption of various kinds of technological systems: satellite [2] and HF radio communications [5] are affected by the increased energy and particle density in the atmosphere and near Earth space; electrical faults can develop on space craft due to anomalous charging [1]; and power grids, oil pipelines and ground-based telecommunication are affected by low frequency currents induced by the changing geomagnetic field [3,16]. Due to the adverse effects that damage to critical technological infrastructure can have on modern society, major efforts are being made to effectively monitor and predict space weather and its impact on specific technologies [14,13].

The intervals of geomagnetic activity that routinely causes the most intense disturbances are known as geomagnetic storms [6] – prolonged periods of significant perturbation to the geomagnetic field usually driven by CMEs. The intensity of geomagnetic storms are quantified by the net disturbance to the field, measured on Earth by any of the dedicated geomagnetic observatories found on all six continents [8]. There are several indices derived from magnetic field measurements to quantify certain aspects of the disturbances. In this work we use the symmetric H index (Sym-H, described in Section 2).

To understand the drivers of geomagnetic disturbances (GMD), characteristic parameters of the solar wind plasma and magnetic field are analyzed. These are measured upstream of the Earth by several satellites [20,19] that orbit the first Lagrangian point (L1) about 1.5 million kilometres upstream of the Earth. Solar wind propagation speed near 1 astronomical unit ($\approx 1.5 \times 10^8$ km; the distance from sun to Earth) range from about 300 km/s (quiet periods) to over 1,000 km/s (severely disturbed), and yields a natural lead time for predictions ranging from about 20 to 90 minutes. Therefore the prediction of some terrestrial index of GMD from measurements taken in the solar wind naturally lends itself to modelling as a regression problem, and as such many attempts have been made to provide forecasts of a variety of disturbance indices tailored to specific space weather effects [15,17,11,7].

Figure 1 shows the progression of a geomagnetic storm over about four days. The top panel shows the Sym-H index and the lower two panels show solar wind parameters measured by the Advanced Composition Explorer (ACE) spacecraft [20]. This storm was due to a single CME impacting the magnetosphere. The passage of ejecta past the spacecraft is recognisable as the increase in density and speed, and the fluctuations in the interplanetary magnetic field (IMF).

A typical geomagnetic storm is seen in the Sym-H curve, starting with the *onset phase* with the arrival of the CME on 17 March, then moving in to the *main phase* as the IMF turns southward ($B_Z < 0$). Southward IMF enables enhanced coupling between the solar wind and magnetospheric plasma, resulting in more efficient energy transfer from the solar wind to the geomagnetic field. After the IMF turns northward ($B_Z > 0$) and the bulk of the disturbed solar wind plasma has passed, the magnetosphere can recover (the *recovery phase* of the storm).

The objective of the solar wind–Sym-H regression model is to use solar wind parameters to predict Sym-H, while taking advantage of the natural lead time afforded by the distance between the space craft and the magnetosphere. In this work, we have an additional goal: to determine whether an analysis of the network can shed light on the physical processes being modelled. We use the solar wind - Sym-H regression problem as test case because the mechanisms of the solar wind - magnetosphere coupling is fairly well understood, and therefore it is known which solar wind parameters are predominantly responsible for driving GMD on the ground. This however, is not the case for more complex problems in space physics and other fields, so this paper serves as an initial proof of concept, before other more complex problems will be tackled in future.

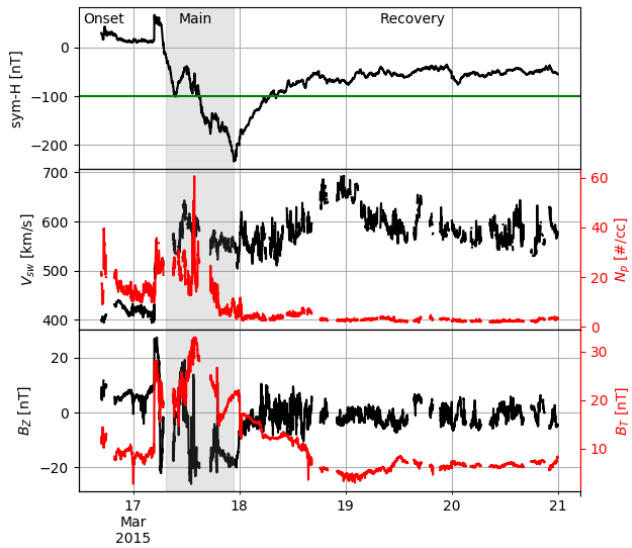

Fig. 1. A typical geomagnetic storm driven by a single CME. The top panel shows Sym-H, with the horizontal green line indicating the -100 nT level. The entire event from start to end is used to develop the model, as is the case for the other 96 storms identified between 2000 – 2018. The lower panels show solar wind parameters V_{sw}, N_p, and B_Z, B_T respectively. The shaded area indicates the main storm phase. The intervals before and after the main phase are identified as the onset and recovery phases, respectively.

With this in mind, we revisit the regression problem (where we task a feed-forward neural network to predict Sym-H from solar wind parameters) with two important changes: Firstly, an adapted network topology is designed to enable the pairwise analysis of input parameter weights. Consider the problem of having access to data from m input parameters $(x_1, x_2, \ldots, x_m)$ that are used to estimate y through some transfer function $\mathcal{F}$:

$$y \approx \mathcal{F}(x_1, x_2, \ldots, x_m) \tag{1}$$

There are various ways of pruning Equation 1 so that those inputs that do not add any value to the model are removed, but these require separate models such as random forests or exhaustive iterations through the possible combinations of inputs [9]. In this work a novel FFNN topology is introduced. The "pairwise" network has input nodes paired up in their connections to the hidden layer (see Section 4.1). This enables input parameter pairs to be ranked during model development, thus reducing user interaction overhead and development time.

The second change is the use of storm phase information as an additional input to the model. It is known that different physical phenomena are at play during different phases of a geomagnetic storm. We show that simply including

phase information in the set of input parameters improves prediction performance. Finally we show how the input parameter rankings change when restricting the model to only one storm phase, further demonstrating the utility of analysing parameter importance to gain insight into the problem at hand, beyond merely seeking accurate predictions.

2 Input and output parameters

Before we introduce the data set itself, we describe the physical quantities used as input to the task, as well as the construction of the Sym-H index.

2.1 Solar Wind Parameters

Solar wind data is collected from the High Resolution OMNI data set [18]. Measurements taken at 16 or 64 second cadence (depending on the instrument) are averaged to 1-minute values and shifted in time to the estimated position of the magnetospheric bow shock nose (BSN) [18]. This ensures that the propagation time from L1 to the BSN does not have to be incorporated into model development. Several plasma and magnetic field parameters are included in this study, all contributing to some extent to the dynamics involved in driving a geomagnetic storm:

V_{sw} Solar wind speed [km/s] is the bulk speed of the plasma moving across the spacecraft.

N_p Proton number density [#/cc] measured in particles per cubic centimetre indicates the particle density of the plasma. Coronal mass ejecta are usually more dense than the ambient solar wind plasma.

P_d Dynamic flow pressure [nPa] is the flow pressure of the solar wind and is linearly related to $N_p V_{sw}^2$.

E_M Merging electric field in the solar wind [mV/m] serves as an indication of the coupling between the solar wind and magnetospheric plasmas and is linearly related to $-V_{sw} B_Z$.

$B_{X,Y,Z}$, B_T The three components of the IMF, measured in nT, and the total field B_T.

2.2 Sym-H index

The target or output parameter to the regression problem is the Sym-H index. This is an index calculated at 1-minute cadence, derived from the horizontal (with regard to the Earth's surface) component of the geomagnetic field measured at 11 middle latitude magnetic observatories. Sym-H serves as an indication of the strength of the *ring current* [12] which circles the Earth and is the main driver of magnetic storm activity on the ground.

3 Data sets

The data set consists of solar wind and Sym-H data, at 1-minute cadence, from the period 2000 – 2018. This period includes almost two full solar activity cycles and is therefore representative of a wide range of geomagnetic storms in terms of drivers and intensity.

3.1 Event selection

Geomagnetic storms are fairly rare events and as such only intense geomagnetic storms, those with minimum Sym-H < -100 nT, were selected out of the 19 year period. Using all available data would result in a very unbalanced data set, with the storm periods being under-represented. The event selection algorithm is described in [10]. Using this method 97 storms are identified, resulting in 396,164 minutes of data (excluding missing values) out of a possible $\sim 9.9 \times 10^6$ minutes. The collection of distinct storms are used to divide the data in to training (67 storms), testing (15 storms) and validation (15 storms) sets. Keeping storm intervals separate ensures that the three sets are truly independent – every storm interval is wholly contained in only one of the three data sets. The training set is used during training to adapt weights through the backpropagation algorithm, the validation set is used to determine the model's performance after each epoch, and the test set serves as the independent out of sample data set on which the model's performance is ultimately calculated. The entire data set is standardized by removing the mean and scaling to unit variance.

Within each storm, the onset, main and recovery phases are identified by searching for the (i) interval around the positive increase in Sym-H (onset phase), (ii) the rapid decrease to storm minimum (main phase), and finally the (iii) recovery period from the minimum Sym-H until the end of the event. These identifiers are important because there are different physical processes involved in the various storm phases.

4 Model development

Two different types of architectures are utilised, a standard fully-connected FFNN and a "pairwise" neural network, detailed below (Section 4.1). The same process is utilised to optimize all networks, as described in Section 4.2.

4.1 The Pairwise net

A fully-connected feedforward network layout mixes signal from all inputs as information flows through the hidden layers to the output. This enables the training procedure to utilise all the different combinations of input parameters to find an efficient solution. Analysis of these sets of combinations are prohibitively complicated since from the first layer of hidden nodes, every node is directly or indirectly connected to every input parameter. Selectively removing some

connections from the input layer to the first hidden layer results in distinct combinations of inputs to be fed to the subsequent hidden layers of a network.

In this work we introduce the "pairwise" network, constructed by the following procedure. Given a model with M input parameters, H hidden nodes in a single hidden layer, and K output nodes:

1. Find all possible distinct pairs of inputs $\{X_i, X_j\}$ $(i \neq j)$ in the list $\{X_1, X_2, \ldots, X_N\}$. Say there are P such pairs, and note that $\{X_i, X_j\} \equiv \{X_j, X_i\}$.
2. Divide the set of hidden nodes in to P distinct groups.
3. Fully connect each pair of inputs to its corresponding group of hidden nodes.
4. Fully connect all the hidden nodes to the output nodes.

The pairwise net is described with an example problem where N_p, V_{sw} and B_T are used to estimate P_d. Figure 2(a) shows the layout, with connections coloured by input parameter to aid the visualisation.

Input parameter ranking is performed by tracking the sum of normalised weights at every training epoch for the pairs of inputs in the pairwise network. The idea behind this method follows naturally from how neural networks are trained. During back-propagation, weights are updated according to their gradient, i.e. their influence on the loss value. Weights that improve the loss are amplified and weights that worsen the loss value are attenuated. With this in mind, the combination of weights in the final layer of the pairwise model becomes a measure of the preceding sub-network's importance to the output value of this regression problem. Weights are first normalized across the network to ensure that the values of weights in the last layer can be compared. Similar to [4], we calculate the norm of the fan-in weight vector at each node and divide the fan-in weights and multiply the fan-out weights with this value. This has no effect on the function the network represents but ensures that the weight values are comparable per layer. In practice, the sum of weights are averaged over several seeds.

In this example we know the pair (V_{sw}, N_p) should yield the highest sum of weights, since $P_d \sim N_p V_{sw}^2$, and the pairs that include the less useful input B_T are suppressed by the training algorithm. This is indeed what happens, according to the weights plotted in Figure 2(b): the sum of weights dominate for pair (V_{sw}, N_p), while the other two pairs are suppressed.

4.2 Parameters and procedure of model development

Two distinct network layouts are investigated in this work: feedforward networks and the pairwise net layout described above. The baseline model (hereafter labelled B_1) is a fully connected FFNN with solar wind parameters as input and Sym-H as output. Model B_1 is trained with the 8 solar wind inputs, two hidden layers of 10 nodes each and a single output node (Sym-H).

Since different physical processes are at play during the three storm phases, categorical input parameters are created to indicate phase. The relevant phase indicator is set to 1 when the appropriate phase (onset, main or recovery) is in

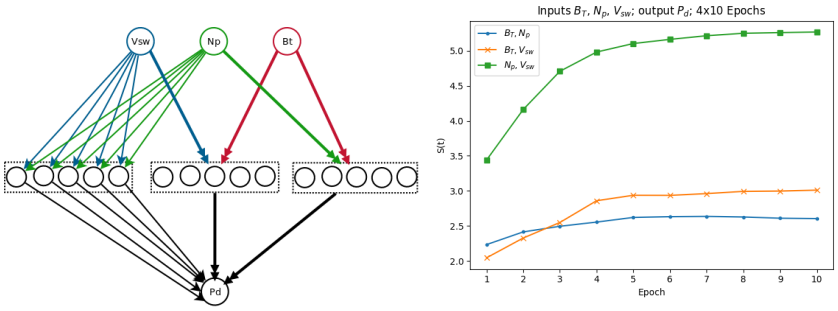

(a) Pairwise network layout. The double-headed arrows indicate full connection (for picture clarity).

(b) Weight evolution over 10 epochs of training.

Fig. 2. Pairwise network with three inputs and one output. Dynamic pressure P_d is predicted by three parameters, B_T, V_{sw} and N_p, while it is known that only two of them are useful (V_{sw} and N_p).

progress, and set to 0 at other times. Therefore, model B_2 has $8 + 3 = 11$ input parameters.

A further improvement is made by adding temporally shifted versions of each parameter to the set of inputs. For each input parameter X_t, measured at time t, another input X_{t-m} is added, doubling the number of inputs of model B_3 to 16. The magnetosphere has a measure of "memory" in that the magnetohydrodynamic processes that govern the storm time phenomena take some time to react and recover from solar wind energy input [12]. In this case we let $m = 270$ minutes, chosen by a parametric search of shifts. Applying this time shift resulted in a marked increase in performance (see Section 5).

Various pairwise network models are developed. A simple model with the 8 solar wind inputs and 10 hidden nodes in 2 hidden layers is trained (P_1), and is shown to perform as well as model B_1. This shows that the pairwise nodes do not reduce performance for this application. Subsequent pairwise models are developed by adding phase and time-shifted parameters (P_2 and P_3).

Both the B_i and P_i models are trained with Adam as the optimizer and mean squared error as the loss function. Correlation between the predicted and observed output is used as a performance metric. All optimization decisions are based on the model's performance on the validation set. Early stopping is implemented by selecting models with the largest validation correlation. Extensive probing showed that weight decay, batch normalization and learning rate schedulers make little to no improvement to the performance, therefore none of these are used. It was also found that smaller mini-batches have better performance, so a mini-batch size of 64 is chosen. Increasing the network width or depth does not improve performance, therefore the mentioned network sizes are chosen as such in favour of computational efficiency. A grid search is done to determine the best learning rate. Three initialization seeds are considered for both the B_i

and the P_i models. The test results of these models are listed in Table 1 and discussed in the next section.

5 Results

5.1 Baseline model

Without phase or time-shifted inputs, the optimal baseline model (B_1) has a 0.63 test correlation. By adding phase (B_2) or time-shifted inputs (B_3), the performance increases to 0.79 and 0.76, respectively. With both phase and time-shifted inputs added (B_4), the model reaches a test correlation of 0.83.

Figure 3 shows an example of Sym-H predicted by models B_1 and B_4 during a geomagnetic storm. It clearly shows the advantage of adding phase information and time-shifted parameters to the set of inputs, especially during the onset and recovery phases.

Table 1. Model performance for the different model types.

Model	Description	Layout	Test Corr.	S.E.
B_1	FFNN	8:(10,10):1	0.63	0.0008
B_2	FFNN with phase	(8+3):(10,10):1	0.79	0.0081
B_3	FFNN with time-shifted inputs	(8+8):(10,10):1	0.76	0.0100
B_4	FFNN with phase and t-shifted inputs	(8+3+8+3):(10,10):1	0.83	0.0047
P_1	Pairwise net	8:(10,10)[a]:1	0.66	0.0066
P_2	Pairwise net with phase	(8+3):(10,10)[a]:1	0.81	0.0022
P_3	Pairwise net with time-shifted inputs	(8+8):(10,10)[a]:1	0.77	0.0022
P_4	Pairwise net with phase and t-shift	(8+3+8+3):(10,10)[a]:1	0.81	0.0056

[a] Hidden layers of the pairwise model's sub-networks

5.2 Pairwise net

With no phase information or time-shifted inputs (P_1), the best model has a 0.66 correlation on the test set. By adding phase (P_2) or time-shifted (P_3) inputs, the validation correlation increases to 0.81 and 0.77, respectively. With both phase and time-shifted (P_4) inputs, the test correlation is 0.81.

5.3 Input parameter ranking through pairwise net

The pairwise net P_1 is developed with (i) the entire data set, and (ii) with the dataset divided according to the three storm phases. This enables the ranking of input pairs in general and for separate storm phases. This is to see if the input ranking via the pairwise nets reflects the known differences in physical phenomena at play during the different storm phases. In both cases the best performing

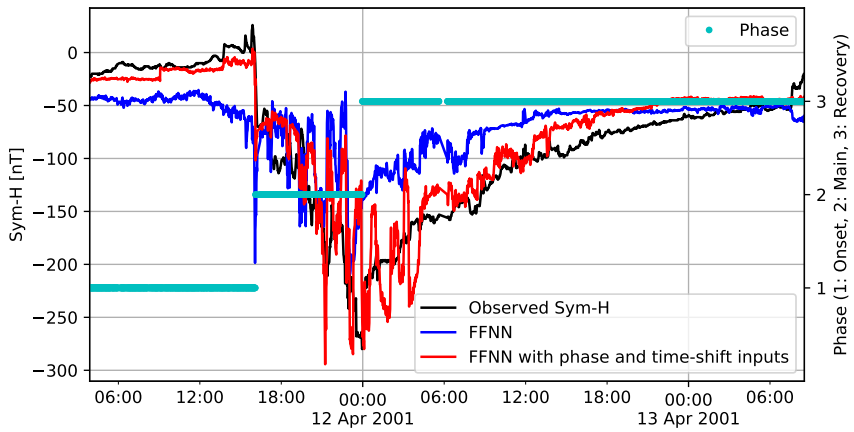

Fig. 3. Predicted and observed Sym-H values during a geomagnetic storm. Model prediction results are shown both with and without phase and time-shifted inputs. The different storm phases are also indicated here.

pairwise model is used. Ranking is done by taking the sum of absolute normalized weights on the epoch where the model achieved its best validation performance. The results are then averaged over 4 iterations with different initialization seeds. All 8 input parameters are considered in pairs of 2. Table 2 shows the resulting average sum S of absolute normalized weights after the last epoch, for the top ranked and bottom ranked input pairs.

6 Discussion and Conclusions

6.1 Model performance

This investigation confirms that neural networks are a viable option for predicting a geomagnetic storm index (i.e. Sym-H) only from solar wind parameters. The simplest model are able to reach a test correlation of 0.63. By adding phase and temporal information, the performance increases to 0.83.

The proposed pairwise network achieved approximately the same predictive performance as the simple baseline neural network, with the added benefit of ranking the importance of input parameters.

6.2 Interpretation of the input parameter selection

The pairwise nets enable a crude form of input parameter ranking, built in to the framework of a fully connected FFNN, without the need for explicit ranking procedures. The sum of absolute normalized weights S at the final epoch is listed

in Table 2. It shows the top-ranked and bottom-ranked input pairs for all phases and is then separated by phase.

The first pair of columns in Table 2 lists the input pairs arranged by S for the entire data set (i.e. all storm phases). The remaining three pairs of columns lists inputs pairs with their respective S for each storm phase.

For entire storms the most influential pair of inputs is (V_{sw}, E_M). Both of these parameters serve as general indicators of geoeffective solar wind activity. Geomagnetic storms are broadly characterised by sudden increase and subsequent gradual decrease in solar wind speed, and E_M is a proxy for the energy input in to the magnetosphere, as it is related to B_Z and V_{sw}. Most of the top-ranked pairs are physically relevant as they are all related to the typical processes involved in geomagnetic storms, such as increased dynamic pressure and solar wind forcing (V_{sw}, P_d and N_p), and reconnection (B_Z and E_M).

The second pair of columns shows the ranking for onset phase. Top ranked are the pairs (B_T, B_Z) and (B_T, E_M) – both of these pairs indicating general increase in activity around onset and the reconnection (indicated by negative B_Z) necessary for storm onset. The lowest ranked pairs are dominated by B_X and B_Y which are not very influential in storm development.

For the storm main phases E_M and V_{sw} dominate top ranked pairs. The inclusion of B_X in the top pair is slightly puzzling, as according to current understanding of main phase dynamics, it should not play a big role. The bottom ranked pairs include parameters such as density (N_p) with B_X and B_Y.

During storm recovery it is the absence of input from the solar wind that allows the magnetosphere to recover by various wave-particle interactions that allow energetic particle populations to lose energy. Here the top ranking pair of inputs is (B_T, V_{sw}) – both of these parameters serve as general indicators of disturbances in the solar wind. After a CME passes the solar wind speed gradually decreases to ambient level and the fluctuations in the IMF decrease significantly. Both of these are indicators of the solar wind plasma and magnetic field returning to an ambient state.

	All		Onset		Main		Recovery	
Rank	Pair	S	Pair	S	Pair	S	Pair	S
28	B_Y, E_M	0.567	B_X, B_Y	0.241	B_Y, N_p	0.206	B_X, P_d	0.363
27	B_X, B_Y	0.601	P_d, E_M	0.274	B_X, N_p	0.242	B_Y, P_d	0.423
26	N_p, E_M	0.622	B_Y, E_M	0.303	B_Y, P_d	0.246	N_p, P_d	0.432
25	B_X, N_p	0.630	B_X, P_d	0.333	B_X, P_d	0.265	P_d, E_M	0.433
1	V_{sw}, E_M	1.369	B_T, B_Z	0.755	B_X, E_M	0.578	B_T, V_{sw}	0.931
2	B_T, V_{sw}	1.125	B_T, E_M	0.752	V_{sw}, E_M	0.547	V_{sw}, P_d	0.808
3	B_Y, P_d	1.112	V_{sw}, E_M	0.680	B_Z, P_d	0.537	B_T, E_M	0.795
4	B_T, P_d	1.095	V_{sw}, P_d	0.648	B_T, V_{sw}	0.523	B_T, N_p	0.769

Table 2. Sum of weights S for the top ranked (1–4) and bottom ranked (25–28) pairs of inputs, for training set consisting of all data and separated by storm phase.

6.3 Conclusions and further work

In this work we illustrated how domain knowledge can increase the performance of a neural network based model on a well-known regression problem and that smart model design can inform domain knowledge. In this age of rapidly increasing machine learning capability researchers and domain experts need to be cognisant of the dangers of well performing, but un-explainable models.

Revisiting the well-known solar wind–Sym-H regression problem, we showed that adding storm phase and time-shifted solar wind parameters increases model performance, as would be expected given the current understanding of the problem. Then, a novel neural network layout was introduced that allows an, admittedly crude, way of ranking the available set of input parameters. It was shown that (i) the modifications does not decrease performance when compared to a simple FFNN and that (ii) the rankings, calculated by taking the sum of normalised weights, generally agrees with the current understanding of the problem.

Further development of the pairwise network introduced here will concentrate on a more rigorous analysis and interpretation of weight analysis during training, and eventually the application of these ideas to more complex problems.

References

1. Baker, D.N.: The occurrence of operational anomalies in spacecraft and their relationship to space weather. IEEE Transactions on Plasma Science, 28(6), pp.2007-2016 (2000).
2. Béniguel, Y. and Hamel, P.: A global ionosphere scintillation propagation model for equatorial regions. Journal of Space Weather and Space Climate, 1(1), p.A04 (2011).
3. DH Boteler: Assessment of Geomagnetic Hazard to Power Systems in Canada, Natural Hazards, Vol 23, pg. 101 – 120 (2001).
4. Davel, M.: Activation gap generators in neural networks, South African Forum for Artificial Intelligence Research (FAIR 2019), submitted for publication.
5. Frissell, N. A., Vega, J. S., Markowitz, E., Gerrard, A. J., Engelke, W. D., Erickson, P. J., et al.: High-frequency communications response to solar activity in September 2017 as observed by amateur radio networks. Space Weather, 17, 118–132 (2019). DOI: 10.1029/2018SW002008
6. Gonzalez, W. D., Joselyn, J. A., Kamide, Y., Kroehl, H. W., Rostoker, G., Tsurutani, B. T., & Vasyliunas, V. M.: What is a geomagnetic storm? Journal of Geophysical Research, 99(A4), 5771 (1994). DOI: 10.1029/93JA02867
7. Gruet, M. A., Chandorkar, M., Sicard, A., & Camporeale, E.: Multiple-hour-ahead forecast of the Dst indexusing a combination of long short-termmemory neural network and Gaussianprocess. Space Weather,16, 1882–1896 (2018). DOI: 10.1029/2018SW001898
8. Intermagnet Homepage, `http://www.intermagnet.org`. Last accessed 10 Oct 2019.
9. Lotz, S. I., Heyns, M. J., and Cilliers, P. J.: Regression-based forecast model of induced geo-electric field. Space Weather, 15, 2016. ISSN 1542-7390. `http://dx.doi.org/10.1002/2016SW001518`.
10. Lotz, S. I., and Danskin, D. W.: Extreme value analysis of induced geoelectric field in South Africa. Space Weather, 15. doi: 10.1002/2017SW001662 (2017).

11. Lotz, S., Heilig, B., and Sutcliffe, P.: A solar-wind-driven empirical model of Pc3 wave activity at a mid-latitude location. Annales Geophysicae, 33, 225–234, 2015. DOI:10.5194/angeo-33-225-2015.
12. Moldwin, M.: An Introduction to Space Weather, Cambridge University Press (2008).
13. Oughton, E. J., Hapgood, M., Richardson, G. S., Beggan, D., Thomson, A. W. P., Gibbs, M., Horne, R. B. (2018). *A Risk Assessment Framework for the Socioeconomic Impacts of Electricity Transmission Infrastructure Failure Due to Space Weather: An Application to the United Kingdom.* Risk Analysis, (November). `https://doi.org/10.1111/risa.13229`
14. Pecasus, `http://pecasus.eu/`. Last accessed 10 Oct 2019.
15. Siscoe, G., McPherron, R. L., Liemohn, M. W., Ridley, A. J., & Lu, G.: Reconciling prediction algorithms for Dst. Journal of Geophysical Research: Space Physics, 110(December 2004), 1–8. DOI: 10.1029/2004JA010465
16. Trichtchenko, L., & Boteler, D. H.: Modelling of geomagnetic induction in pipelines. Annales Geophysicae, 20(7), 1063–1072 (2002). DOI: 10.5194/angeo-20-1063-2002
17. P Wintoft, Wik, M., Lundstedt, H., Eliasson, L.: Predictions of local ground geomagnetic field fluctuations during the 7–10 November 2004 events studied with solar wind driven models. Ann. Geophys. 23, 3095–3101 (2005).
18. OMNIWeb Homepage, `https://omniweb.gsfc.nasa.gov/`. Last accessed 10 Oct 2019.
19. DSCOVR Homepage, `https://www.nesdis.noaa.gov/content/dscovr-deep-space-climate-observatory`. Last accessed 10 Oct 2019.
20. Advanced Composition Explorer, `http://www.srl.caltech.edu/ACE/`. Last accessed 10 Oct 2019.